Materials & Design 221 (2022) 111014

Contents lists available at ScienceDirect

Materials & Design

journal homepage: www.elsevier.com/locate/matdes

Penetration mechanism of the emulsion-based rejuvenator in damaged porous asphalt mixture: Microstructure characterization and 3D reconstruction

Jiwang Jiang[a], Zhen Leng[a,*], Bin Yang[a], Guoyang Lu[a], Zhifei Tan[a], Meizhao Han[a,b], Zejiao Dong[b]

[a] Department of Civil and Environmental Engineering, the Hong Kong Polytechnic University, Kowloon 999077, Hong Kong
[b] School of Transportation Science and Engineering, Harbin Institute of Technology, Harbin 150090, Heilongjiang, China

HIGHLIGHTS

- The spatial distribution of asphalt emulsion residue in porous asphalt can be back-calculated from X-ray computed tomography scanning images.
- The penetration of asphalt emulsions in damaged porous asphalt presents gradient characteristics in the depth direction.
- Asphalt emulsion reshapes the size, number, area, interconnectivity and tortuosity of air voids in damaged porous asphalt.
- Statistical micro-scale indexes were proposed to indicate the emulsion residue coating efficiency, mortar thickening and spatial homogeneity.

GRAPHICAL ABSTRACT

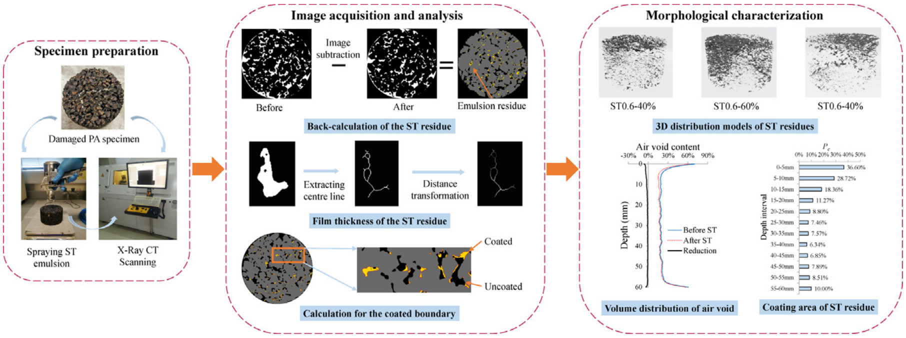

ARTICLE INFO

Article history:
Received 18 March 2022
Revised 28 June 2022
Accepted 31 July 2022
Available online 3 August 2022

Keywords:
Porous asphalt (PA) mixture
Surface treatment (ST)
Penetration
Microstructure
X-ray CT scanning
Image analysis

ABSTRACT

Porous asphalt (PA) pavement suffers from the early-stage raveling problem, which hinders the wide application of this sustainable technology. Several promising attempts have been made to restore the durability of PA wearing courses by using surface treatment (ST) emulsions. However, the working mechanism of the ST emulsion is still unclear. Therefore, this study aims to investigate the penetration behavior of the ST emulsion in damaged PA. X-ray CT scanning was performed to monitor the changes in the pore microstructure of PA specimens under three selected ST conditions. The spatial distribution of ST emulsion residue was back-calculated and 3D visualized through image analysis. The coating efficiencies and thickness distributions of ST emulsions were quantitatively estimated to characterize their penetration status. The analysis results showed that the distribution of ST emulsions in damaged PA presents gradient characteristics with a deepest penetration depth of around 20 mm. The ST application reshaped the interconnected-pore microstructure. The PA specimen treated by ST emulsion with best coating efficiency and thickest coating film showed the best performance recovery among the three ST conditions. The outcomes of this study are expected to help optimize the performance of the ST technology for PA, thus contributing to more durable PA pavements.

---

[*] Corresponding author.

https://doi.org/10.1016/j.matdes.2022.111014
0264-1275/© 2022 The Authors. Published by Elsevier Ltd.

1. Introduction

Porous asphalt (PA), an open-graded asphalt mixture with large air void content, has been widely used as a multi-functional and environmental-friendly road surfacing material in high-density cities, like Hong Kong [1]. The high air void content of PA could provide attractive functions, such as noise reduction [2], excellent skid-resistance [3], rapid water drainage [4], and alleviated urban heat island effect [5]. However, the high air void content also weakens the bearing capacity of the open-graded material structure [6], accelerates the oxidative aging of binder and deterioration of aggregate-binder interface due to moisture diffusion [7,8]. Therefore, compared with conventional dense-graded asphalt mixture, PA usually has shorter service life because of its early raveling distress, which refers to the dislodgement of aggregate particles starting from the pavement surface [9]. The loose aggregates due to raveling not only deteriorate PA but also pose a potential risk to driving safety.

To minimize PA's premature raveling problem, pavement engineers have made considerable efforts, such as using more asphalt binder [10], hydrated lime [11], anti-stripping additives or fibers [12], and innovative binders [13]. According to Japanese experiences, a special polymer modified asphalt containing 9% styrene-butadienestyrene (SBS) with very high 60 °C viscosity can greatly extend the service life of the PA wearing course [14]. Recently, the high-viscosity binder with a Superpave performance grade of 82-22 (PG82-22) has been introduced to Hong Kong to improve the durability of PA wearing course [15]. A trial pavement section adopting both asphalt rubber (AR) and chemically recycled waste polyethylene terephthalate (PET) as the adhesion promotor has also been successfully built in Hong Kong to improve the longevity of PA [16]. Moreover, resin-based asphalt binder modifiers, such as the polyurethane (PU) and epoxy, have been investigated and applied to further improve the mechanical performance and broaden the application of PA [17,18,19,20]. Despite the successful application of different technologies, raveling can hardly be eliminated, and it is still the major distress which limits the service life of PA wearing course.

In addition to improving the PA material itself, adopting appropriate preventive maintenance strategies could also be an effective solution to improve the long-term performance of PA wearing course considering both economic and environmental interests [21]. For conventional asphalt pavement, there are many mature preventive maintenance methods being used for several decades [22], but very few preventive maintenance methods are available for PA wearing course. One potential reason is that the preventive maintenance technologies for dense-graded asphalt pavement (e.g., fog seal, chip seal, and micro-surfacing) may help improve the durability of PA, but at the same time they will also compromise its functional performance, which is unacceptable. In 2010, the Dutch Ministry of Infrastructure and Environment started a feasibility study on preventive maintenance of PA wearing course by spraying the surface treatment (ST) emulsions [23]. It was verified that the ST emulsion could improve the raveling resistance of the in-service PA pavement without clogging voids. Zhang et al [24,25] further evaluated the effects of the extra bio-based and petrol-based rejuvenators in the ST emulsion on the performance recovery of the artificially aged asphalt mortar, by assuming that rejuvenators may diffuse into and soften the aged binder. Xu et al [26] investigated the recovery efficiency of four different rejuvenating materials and the more effective rejuvenator was identified by raveling resistance evaluation. However, despite the positive outcomes of the studies and applications of ST emulsion for PA wearing course, most of these outcomes are based on macroscopic laboratory tests and empirical field trials, while the fundamental studies on the interaction mechanism between the ST emulsion and PA are still very limited.

To understand such a mechanism, it is important to know how the emulsion penetrates the pore structure and how the ST emulsion residue is distributed spatially in damaged PA. ST emulsions are liquids with certain viscosities during the penetration stage. Several studies have been conducted to characterize the clogging [27] or water flow [28] of PA at the micro-scale using the image analysis approach, which are solid particle and pure water penetration process, respectively. For the interaction between the ST emulsion and PA, it is expected that the additional emulsion residue may fill some micro-cracks and thicken the aged asphalt binder film, but no quantitative evidence is available. To fill this gap, this study aims to: 1) morphologically characterize the 3D microscopic pore structure of the PA under different ST conditions through image analysis; 2) back-calculate the 3D spatial distribution of the ST emulsion residue within the damaged PA; and 3) quantitatively estimate the penetration status of the ST emulsion by the newly proposed micro-scale indexes.

2. Materials and methodology

2.1. Laboratory testing program

2.1.1. Materials and mixture design

An open-graded asphalt mixture with a nominal maximum aggregate size (NMAS) of 13.2 mm, named PA-13, was selected for this study. The aggregates used were granite and the asphalt binder was SBS modified asphalt binder with a Superpave performance grade of 76-16 (PG76-16). Besides, the hydrated lime with a content of 1.5% by weight of aggregate was added to improve the moisture resistance of PA-13. The optimum asphalt content was determined to be 3.9% by weight of the asphalt mixture and the target air void content was 23 ± 0.5% in accordance with the Chinese standard JTG/T 3350–03-2020 [29]. The detailed gradation and volumetric information are shown in Table 1. A cationic slow-setting (CSS-1) type asphalt emulsion was selected to be the ST emulsion. Based on the preliminary test results, three ST conditions with different emulsion application rates and solid contents were considered in this study, as shown in Table 2. The solid content refers to the weight of asphalt residue to the total weight of the asphalt emulsion before evaporation.

2.1.2. Specimen precondition and ST application

All PA specimens were subjected to aging and environmental conditioning to create internal micro-damages. The aging condition was set to be oven aging for the loose mix (Fig. 1(a)) at 135 °C for 8 h following the procedures developed by Modified

Table 1
Mix design information of the PA-13.

Sieve size (mm)	Passing percentage (%)		
	Upper limit	Target gradation	Lower limit
16	100	100	100
13.2	100	92.6	90
9.5	71	67.0	40
4.75	30	14.5	10
2.36	20	11.7	9
1.18	17	8.6	7
0.6	14	6.5	6
0.3	12	5.1	5
0.15	9	4.2	4
0.075	6	3.2	3
Binder content (%)	3.9%		
Target air void content (%)	23.0 ± 0.5		

Table 2
Basic properties of the ST emulsion.

Specimen ID	Application rate (kg/m^2)	Solid content (%)	Evaporated residue		
			Penetration (25 °C, 0.1 mm)	Softening point (°C)	Ductility (5 °C, cm)
ST 0.4–60%	0.4	60%	60	64	50
ST 0.6–60%	0.6	60%			
ST 0.6–40%	0.6	40%			

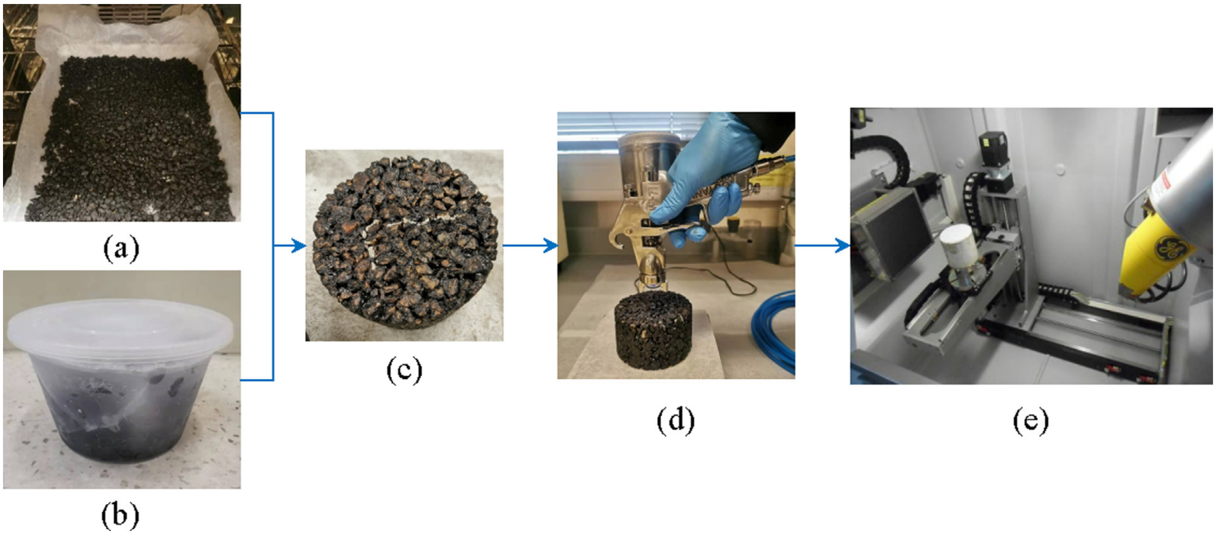

Fig. 1. Laboratory testing procedures: (a) loose mix aging; (b) F-T cycling; (c) damaged SGC specimen; (d) spraying of the ST emulsion; (e) XCT scanning.

Asphalt Research Center in Wisconsin [30]. Then, the aged loose mix was compacted into cylindrical PA specimens with a diameter of 100 mm and a height of 60 mm by the Superpave Gyratory Compactor (SGC). After that, the compacted specimens went through three cycles of Freeze-Thaw (F-T) (Fig. 1(b)) according to AASHTO T283 [31]. Finally, three damaged PA specimens (Fig. 1(c)) were selected for the X-ray computed tomography (XCT) scanning (Fig. 1(e)) before and after ST (Fig. 1(d)) with a curing time of 7 days at room temperature.

2.1.3. Performance verification

The effects of different ST conditions on the performance recovery of the damaged PA were evaluated by the Cantabro Abrasion test [32]. In addition, the permeability coefficients of the damaged PA before and after ST were also measured by a constant head permeameter. Three replicates were prepared for each ST condition. The mass loss ratio and permeability coefficient (K_v) were calculated by Eqs. (1) and (2), respectively. Table 3 presents the detailed test results for different ST application scenarios. The PA specimens with an emulsion application rate of 0.6 kg/m^2 and solid content of 60% provided the highest recovery efficiency. Its permeability coefficient was lower than that of the control material, but still higher than the lower limit of 0.5 mm/s for PA as standardized in EN 12697-19 [33].

Table 3
Performance of the damaged PA before and after different ST application scenarios.

Specimen ID	Mass loss ratio (%)		Permeability coefficient (mm/s)	
	Mean	St.d	Mean	St.d
Control	31.2	2	1.50	0.01
ST 0.4–60%	28.7	4.1	–	–
ST 0.6–60%	17.4	0.7	0.72	0.01
ST 0.6–40%	32.3	2.1	–	–

$$Mass\ \ loss\ \ ratio = \frac{m_1 - m_2}{m_1} \times 100\% \tag{1}$$

$$K_v = \frac{4 \times Q_v \times L}{h \times \pi D^2 \times t} \tag{2}$$

where m_1 = the original mass of the tested specimen, g; m_2 = the mass of the tested specimen after abrasion, g; Q_v = the volume of water that was drained during the test period, mm^3; L = the thickness of the specimen, mm; D = the diameter of the specimen, mm; h = water head, mm; and t = testing period, s.

2.2. Image acquisition and analysis methods

Cross-sectional images of the damaged PA before and after different ST conditions were acquired by an X-ray computed tomography (CT) scanning system of Phoenix v |tome |xs. Table 4 presents the detailed scanning parameters. The horizontal resolutions of different specimens ranged from 0.061 to 0.067 mm/pixel, which could be explained by the slight absorbance variance. The CT slices are 8-bit grayscale images with 256 levels of intensity, which reflect the densities of objects inside the specimen.

2.2.1. Air void identification and morphological analysis

As can be seen in Fig. 2(a) and 2(b), the air void in each CT slice can be separated from the aggregates and asphalt mortar using the image processing methods of enhancement, filtering and thresholding. The white region of the binary image shown in Fig. 2(b) represents the air void of one PA specimen cross-section. Then, the volume, size, and number of air voids in the PA specimen were statistically analyzed considering different ST conditions and scan-

Table 4
Summary of the XCT scanning parameters.

Specimen ID	Scanning timing	Voltage (kV)	X-ray tube current (mA)	Resolution (mm/pixel)	
				Vertical	Horizontal
ST 0.4–60%	Before ST	190	110	0.1	0.067
	After ST				0.061
ST 0.6–60%	Before ST				0.067
	After ST				0.061
ST 0.6–40%	Before ST				0.065
	After ST				0.061

ning timings. The air voids inside PA can be divided into two types: interconnected air voids and closed air voids [34], which have different effects on the flow path of the ST emulsion. Thus, it is important to differentiate the two types of air voids. A series of MATLAB codes were programmed to analyze the interconnectivity of binary images from top to bottom in the vertical direction. As Fig. 2(c) illustrates, a top-down processing program followed by a bottom-up processing was used to distinguish the interconnected air voids from the closed air voids [35]. Each white region in two consecutive CT images was compared starting with the top surface image. If they continuously overlapped from top to bottom, they would be labeled as candidate interconnected air voids. The procedure was then repeated, starting from the bottom surface image, to rule out the closed air voids with a downward dead-end. Finally, the interconnected pores and the closed air voids could be successfully identified. The reconstructed 3D models of both types of air voids are shown in Fig. 2(d) and (e), respectively.

Two indexes, namely interconnected factor (F_i) and tortuosity (T), were used to quantify the interconnectivity of the PA's pore-structure. As Eq. (3) shows, F_i is defined as the ratio of the interconnected air voids to the total air voids, representing the drainage efficiency of the pores in PA. As Eq. (4) shows, T is calculated by dividing the actual length of the flow path by the shortest distance between the two ends of the interconnected porous structure. A larger T value indicates that the movement of the fluid through the interconnected pores is more difficult.

$$F_i = \frac{P_i}{P_t} \times 100 \tag{3}$$

$$T = \frac{L_e}{L} \tag{4}$$

where P_i = the voxel number of the interconnected air void; P_t = the voxel number of all air voids in the specimen; L_e = the distance between the centroids of two interconnected air voids from two target images, mm; and L = the shortest distance between the two images, mm.

2.2.2. Back-calculation of the ST emulsion residue

It is assumed that the volume of the ST emulsion residue is equal to the volume of the reduced air void regions in PA. Based on this assumption, the ST emulsion residue was back-calculated using a set of customized MATLAB codes. The corresponding CT images of PA before and after ST were determined by feature matching. As Fig. 3(a) and (b) illustrate, the original binary images were resized to the same resolution and the center of both circular cross-sections were relocated to the same position. Following that, a rotation operation was performed on the binary images of the treated PA specimen. It should be noted that the rotated angle and center position should be calculated backward by maximizing the overlap between the white areas of the corresponding binary images before and after ST. Finally, through image subtraction, the ST emulsion residue could be successfully identified as shown in Fig. 3(c). The gold area represents the ST emulsion residue, the black area represents the air voids after ST, and the gray area represents the coarse aggregates and mortar in PA specimen.

2.2.3. Film thickness and coating area of the ST emulsion residue

All the ST emulsion residue in the cross-sectional images from the top surface to the bottom were highlighted and labeled. The ST emulsion residues are randomly dispersed over the surface of the aged mortar, as illustrated in Fig. 4(a), but not all of them are fully coated. To quantify the coating efficiency of the ST emulsion

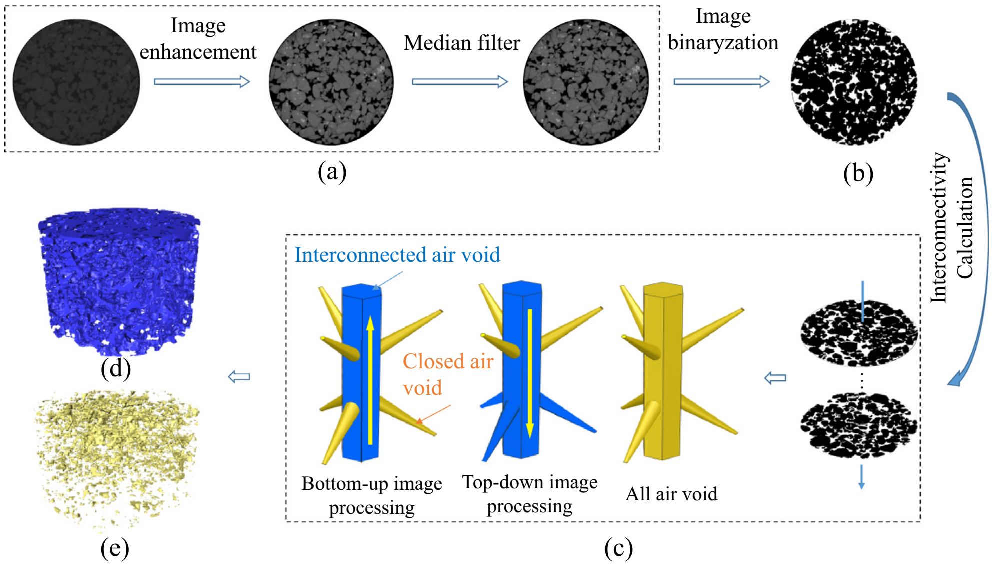

Fig. 2. Procedures for air void identification from the CT slices: (a) pro-processing; (b) binary image; (c) interconnectivity analysis; (d) interconnected air void and (e) closed air void.

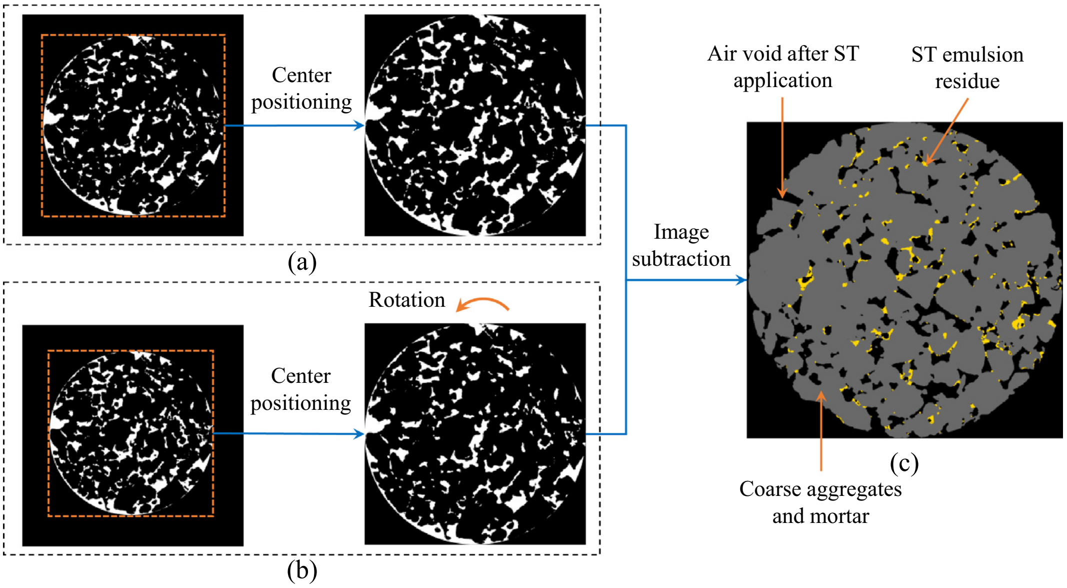

Fig. 3. Images of: (a) air voids before ST; (b) air voids after ST; and (c) ST emulsion residue.

residue, a new index called the percentage of coating area (P_c) was proposed and calculated by Eq. (5). For each CT slice, it is defined as the ratio of the coated boundary length to the total boundary length of the air voids before ST. As Fig. 4(b) illustrates, the coated boundary was marked in red, which is the shared boundary between the aggregates or mortar (gray area) and the ST emulsion residue (gold area).

Besides, as can be seen in Fig. 4(a), the shapes of the emulsion droplets are complicated, and the thickness values of the coating layer on the aged mortar vary. Therefore, the coating film thickness was calculated to quantify the spatial distribution of the ST emulsion residue. A similar approach has been implemented to effectively investigate the meso-structure of the asphalt mortar [36]. A series of image-related MATLAB algorithms were implemented to collect the coating film thickness, as shown in Fig. 4 (c) and (d). The binary images of the ST emulsion residue were first prepared. Then, the centre line of each emulsion droplet was extracted. After that, a distance transformation was applied on the centre line to calculate the shortest distance between the centre line pixels to the boundary of the corresponding droplet. As shown on the right side of Fig. 4(d), the centre lines were assigned with different grayscales to represent different distance values, with darker indicating shorter distance. Finally, the coating film thickness was determined as twice the shortest distance. For each CT slice, thousands of coating film thickness values were collected from different centre line pixels. Two parameters, namely the mean value (T_c) and standard deviation (SD_c), were introduced to characterize the distribution of the coating film thickness.

$$P_c = \frac{\sum_{i=1}^{i=n} L_c^i}{\sum_{i=1}^{i=n} L_a^i} \times 100 \tag{5}$$

where n = number of CT slices; L_c^i = length of the coated boundary for number i image, mm; and L_a^i = boundary length of the air voids before the ST condition for number i image, mm.

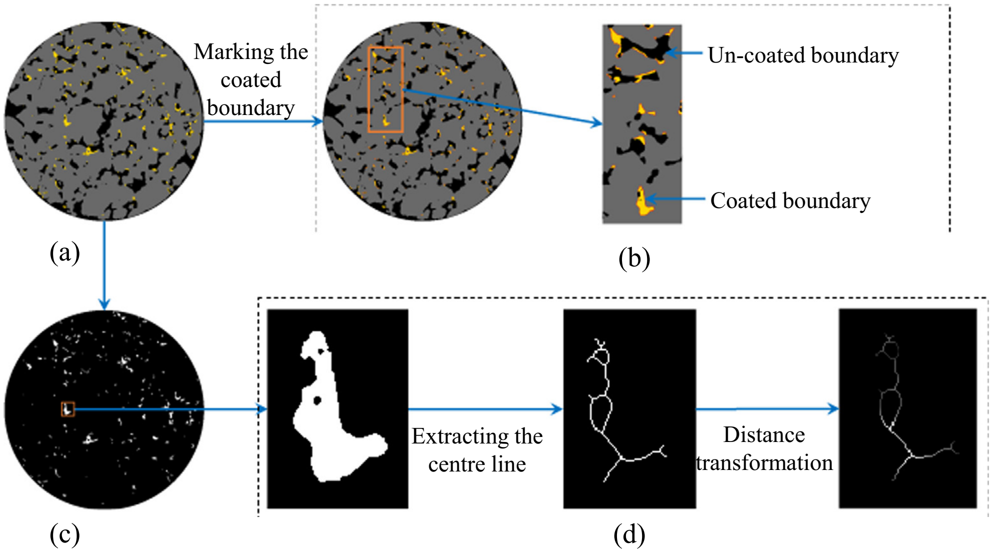

Fig. 4. Calculation methods for the coating area and film thickness of the ST emulsion residue: (a) RGB image; (b) coated boundary; (c) binary image of the ST emulsion residue; and (d) thickness counting.

3. Results and discussions

3.1. Air void reduction in the depth direction

The addition of ST emulsions occupies certain portion of the air voids. The air void content of each CT slice is equal to the area proportion of the white area to the total cross-sectional area. Fig. 5 illustrates the air void content of PA before and after ST as well as the decreased air void content induced by the ST emulsion residue. The vertical volume distribution of the air void in PA before and after ST are both in bathtub shape, which is consistent with the findings of the previous study [37]. Fig. 5 also shows that the distribution of the ST emulsion residue in PA has a vertical gradient profile, with more accumulating near the top of the specimen. The black lines immediately surged around the bottom in Fig. 5(b) and (c), suggesting that only a tiny proportion of the ST emulsion could travel through the interconnected flow path, and it is still reasonable to deduce that majority of the ST emulsion has limited penetration depth. As shown in Fig. 5(b), the majority of the ST emulsion could penetrate approximately 20 mm, but for the other two ST conditions (Fig. 5(a) and (c)), the ST emulsion could only penetrate nearly 10 mm.

In Fig. 5, the absolute values of the air void reduction are quite small and may relate to the value of the total air void content. So, the percentage reduction in air voids (P_{ra}) was also calculated using Equation (6) to further characterize the air void decreasing patterns for different ST conditions. P_{ra} is defined as the ratio of the reduced air void content to the total air void content without ST. Fig. 6 shows the P_{ra} of the PA specimens subjected to different ST conditions with a depth interval of 5 mm. P_{ra} is larger than 5% when the penetration depth is less than 25 mm for ST 0.6–60% condition, but only 10 mm for ST 0.6–40% condition and 5 mm for ST 0.4–60% condition.

$$P_{ra} = \frac{\sum_{i=1}^{i=n}\left(V_{tb}^{i} - V_{ta}^{i}\right)}{\sum_{i=1}^{i=n}V_{tb}^{i}} \times 100 \tag{6}$$

where n = number of CT slices; V_{tb}^{i} = air void content of number i image before ST condition, %; and L_{ta}^{i} = air void content of number i image after ST condition, %.

3.2. Pore morphology of PA before and after ST

The air void contents (V_a) of the three damaged PA specimens before ST were measured by the dimensional method [38] as shown in Table 5. The total and interconnected V_a of PA before and after ST calculated through the image analysis are also presented. Besides, to characterize the size and number of the air voids within the PA specimen, the average equivalent diameter (D_e) and number of air voids (N_a) are also summarized in Table 5. The equivalent diameter of each air void is defined as the diameter of an equivalent circle that has the same area as the air voids. The overall interconnected factor (F_i) and tortuosity (T) were also calculated as presented in Table 5. The V_a values calculated by the CT image processing are all slightly less than those measured by the dimensional method, which may be caused by the limited resolution of CT images [39]. After ST, both the total and inter-connected V_a of the PA specimens decreased with the deviations ranging from 0.7% to 1.4% and 0.9% to 1.7%, respectively. Accordingly, the F_i values of each PA specimen also decreased after ST with varying devi-

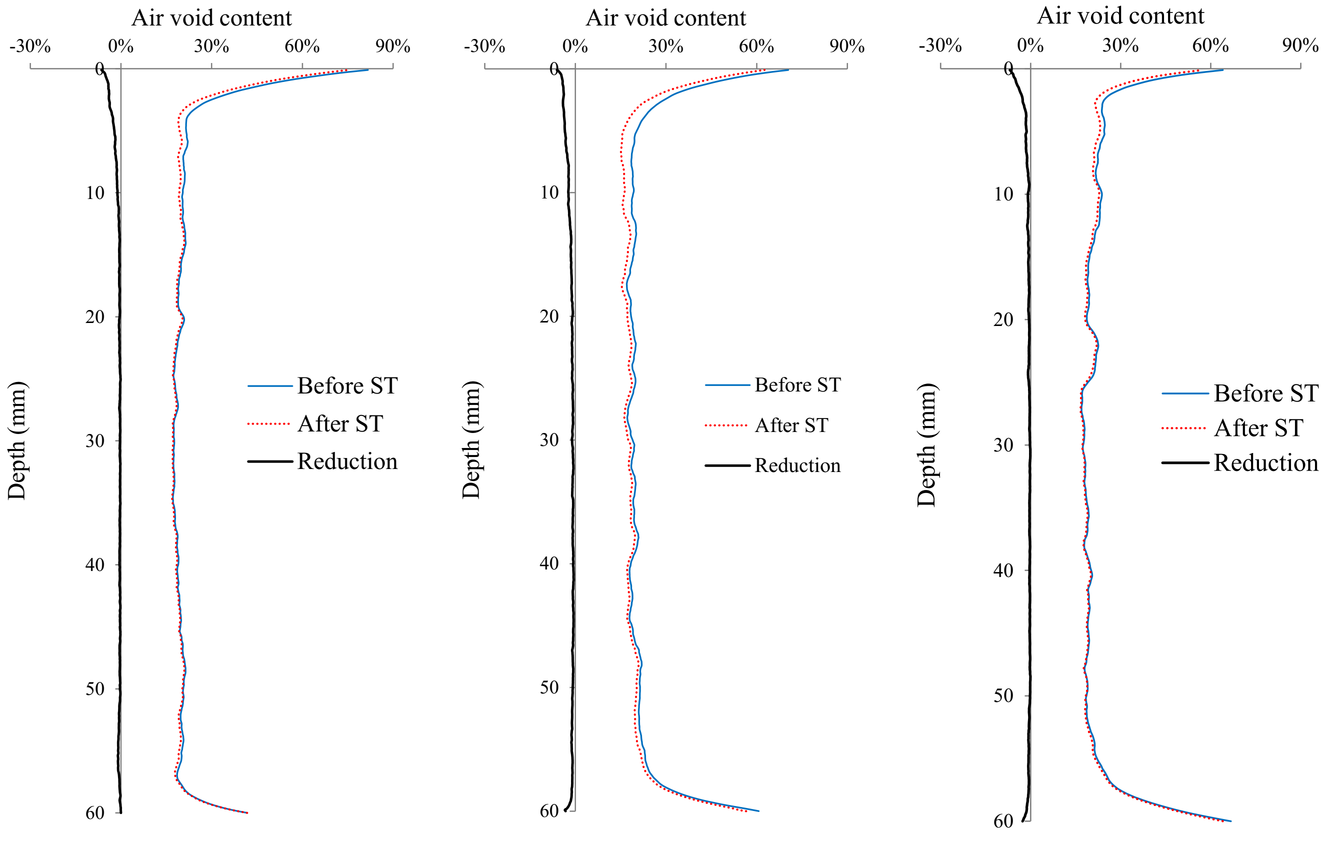

(a) (b) (c)

Fig. 5. The gradient distribution of the air void content along the depth direction before and after different ST conditions: (a) ST 0.4–60%; (b) ST 0.6–60%; and (c) ST 0.6–40%.

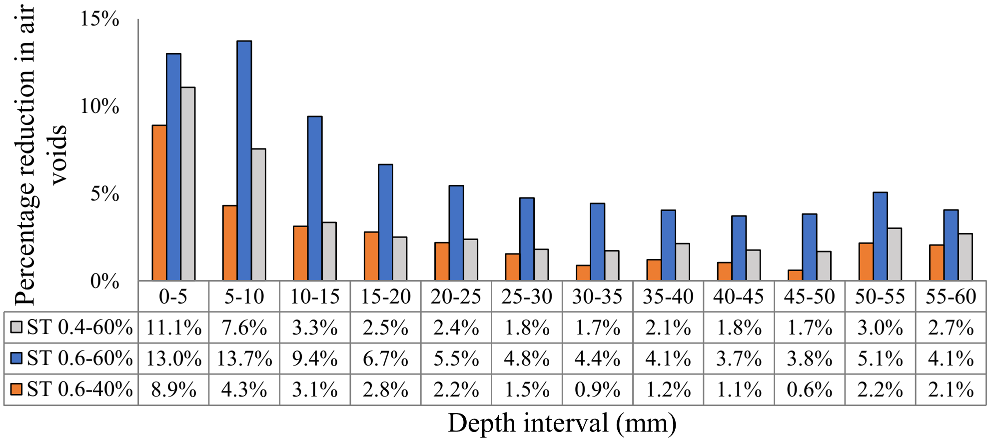

	0-5	5-10	10-15	15-20	20-25	25-30	30-35	35-40	40-45	45-50	50-55	55-60
☐ ST 0.4-60%	11.1%	7.6%	3.3%	2.5%	2.4%	1.8%	1.7%	2.1%	1.8%	1.7%	3.0%	2.7%
■ ST 0.6-60%	13.0%	13.7%	9.4%	6.7%	5.5%	4.8%	4.4%	4.1%	3.7%	3.8%	5.1%	4.1%
■ ST 0.6-40%	8.9%	4.3%	3.1%	2.8%	2.2%	1.5%	0.9%	1.2%	1.1%	0.6%	2.2%	2.1%

Fig. 6. Percentage reduction in air voids (P_{ra}) of PA due to ST in depth direction.

ations, indicating varying effects of ST on the permeability of PA. In addition, after ST, D_e of each PA specimen decreased, while N_a increased, indicating that more air voids with smaller D_e showed up in the treated PA specimen. As for the tortuosity, after ST, the T value of each PA specimen reduced somewhat, so the penetrated ST emulsion may first block or fill the branches along the flow path with little impact on the main fluid channels. Overall, it is noticed that the ST 0.6–60% specimen had the most significant change in all morphological indexes after ST.

3.2.1. Size, number and area distribution of the air voids

Based on the air void volume analysis, it can be confirmed that the penetration of the ST emulsion shows gradient characteristics. Taking ST 0.6–60% as an example, the D_e and N_a values of the air voids in PA before and after ST were further statistically analyzed along the depth direction with an interval of 5 mm as shown in Fig. 7. After ST, the top 20 mm of PA specimen presents decreasing D_e but increasing N_a. The middle 20 mm of PA specimen presents relatively minor fluctuation of D_e and N_a. For the bottom 20 mm, D_e showed an increasing trend while N_a decreased. Therefore, the size distribution of the air voids in PA should have different changes at different depths. To further characterize the effects of ST emulsion residue on the pore structure, the area percentage of the air voids in each CT slice less than 25 mm^2, falling between 25 and 200 mm^2 and larger than 200 mm^2 were counted as shown in Fig. 8. The counting was conducted for PA specimen before and after ST with a depth interval of 20 mm. By contrast, the area percentage of the air voids less than 25 mm^2 increased sharply for the top 20 mm, and considering that N_a also increased, it could be inferred that some large air voids (greater than25 mm^2) were partially occupied by the ST emulsion residue and became smaller or were separated into several smaller ones. For the bottom 20 mm, the area percentage of air voids falling between 25 and 200 mm^2 decreased, and given that N_a also decreased but D_e increased, it could be inferred that some medium size air voids (25–200 mm^2) were totally filled by the ST emulsion.

3.2.2. Typical profiles of the air voids at different depths

The micro-pore structure of PA is affected by the ST emulsion, and the penetration process has obvious gradient characteristics. To better illustrate such an effect, several typical profiles of the air voids after the application of ST 0.6–60% were randomly selected as presented in Fig. 9. The black area is the air voids after ST, and the gold area is the back-calculated ST emulsion residue. Fig. 9(a) is one of the profiles of the treated PA at the depth of 9.9 mm from the top surface. It can be observed that several large air voids, marked by the red circles, were partially filled by the ST emulsion residue and were turned into several smaller voids. As Fig. 9(b) shows, for the middle part of the specimen, most of the ST residue can only fill the micro-pores around the main pore-structure because a limited volume of ST emulsion could penetrate to and remain in this depth. As Fig. 9(c) demonstrates, the ST emulsion residue around the bottom part could completely fill some small air voids while leaving most of the big pores intact. The observation from the typical profiles could well verify the findings obtained from the size, number and area analysis for air voids, and it can be concluded that the penetrated ST emulsion would definitely reshape the micro-pore structure, which is supposed to be one of the key factors influencing the mechanical and functional performance of the damaged PA [40,41].

3.2.3. Interconnectivity and tortuosity of the air voids

The overall interconnectivity and tortuosity of the air voids in PA after ST are also changed. For example, the F_i and T values along

Table 5
Summary of the morphological properties of the air voids in PA.

Specimen ID		Measured V_a	V_a of the images	Inter-connected V_a	Mean value of each CT slice			
					D_e (mm)	N_a	F_i	T
ST 0.4–60%	Before ST	22.7%	21.2%	19.8%	2.375	179	0.932	1.403
	After ST	--	20.4%	18.9%	2.286	183	0.924	1.384
	Deviation	--	0.8%	0.9%	0.089	−4	0.008	0.019
ST 0.6–60%	Before ST	23.1%	21.6%	20.2%	2.461	157	0.944	1.454
	After ST	--	20.2%	18.5%	2.339	162	0.914	1.403
	Deviation	--	**1.4%**	**1.7%**	**0.122**	**−5**	**0.030**	**0.051**
ST 0.6–40%	Before ST	22.8%	22.0%	20.8%	2.388	162	0.934	1.424
	After ST	--	21.3%	19.9%	2.310	164	0.929	1.418
	Deviation	--	0.7%	0.9%	0.078	−2	0.005	0.006

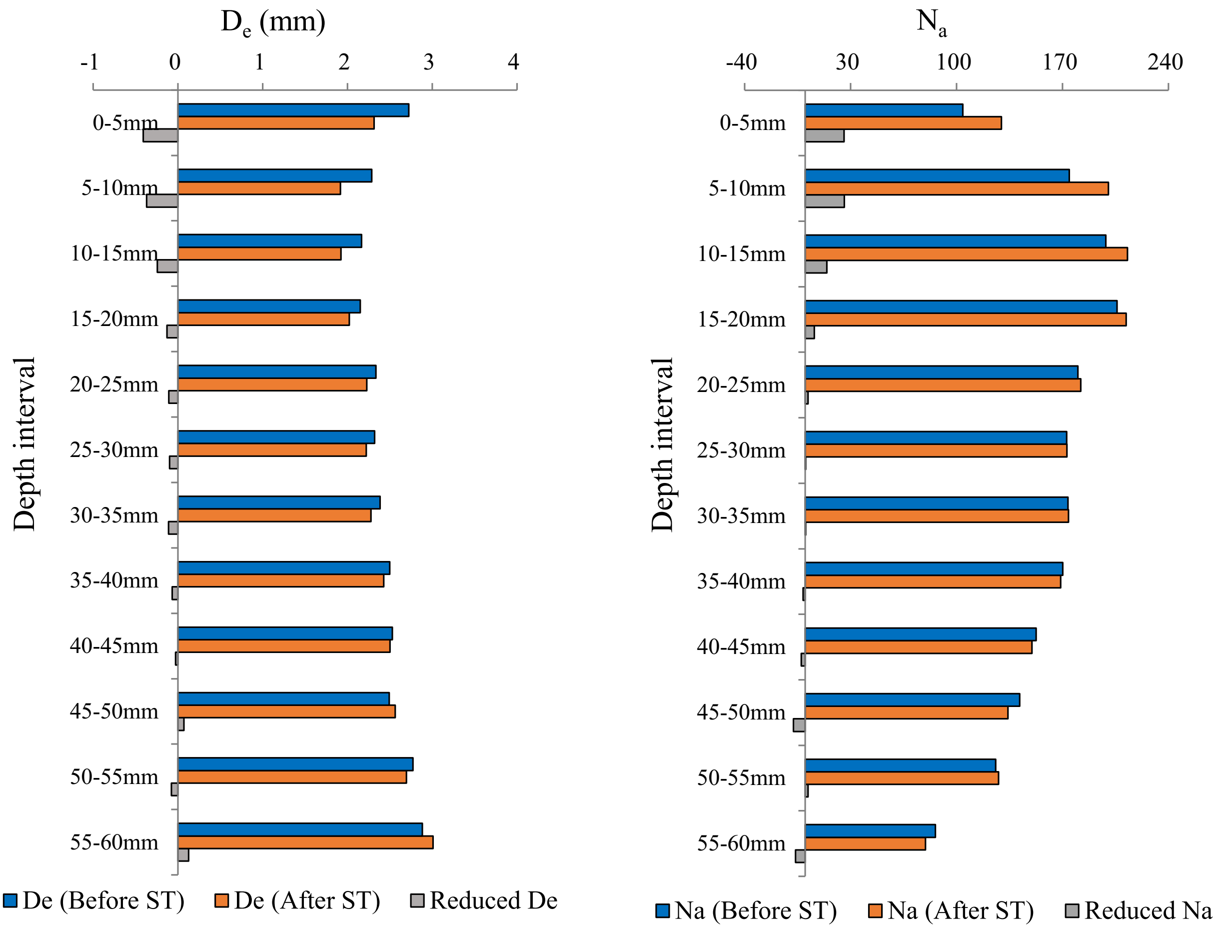

(a)

(b)

Fig. 7. Morphological properties of air voids in PA before and after the ST 0.6–60% condition: (a) D_e; (b) N_a.

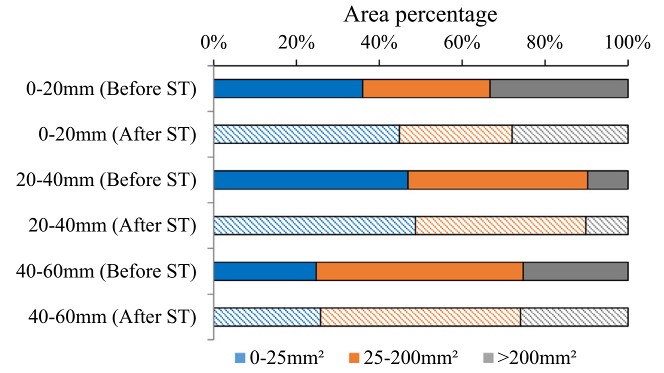

Fig. 8. The area distribution of the air voids in PA before and after the ST 0.6–60% condition.

the depth direction for the specimen of ST 0.6–60% are shown in Fig. 10. As illustrated in Fig. 10(a), after ST, the F_i value presents a significant drop when the depth is less than 20 mm, while keeping almost the same when the depth is more than 20 mm. Fig. 10 (b) shows the tortuosity of the PA specimen before and after ST. The distribution of the T value varied in the range of 1 to 2 due to the inhomogeneous structure of the interconnected pore. After ST, the T value decreased at both ends of the PA specimen. The flow path with higher F_i and lower T values should have better permeability [34]. Therefore, the reduced permeability caused by the ST emulsion should be mainly attributed to the lower F_i near the top portion of the PA specimen.

3.3. Back-calculated distribution of the ST emulsion residue

3.3.1. 3D model visualization

The 3D models of the ST emulsion residue within the PA specimens were reconstructed by stacking the continuously back-calculated binary images of the ST emulsion residue. Based on the visualization shown in Fig. 11, most of the ST emulsion residues concentrated near the top surface of the PA specimens. The shape of the residue droplet is complex and the distribution is non-uniform.

3.3.2. Coating area gradient

Apart from the changed pore-structure, it is also expected that the soft emulsion residue could coat and adhere to the surface of the aged mortar. More coating area indicates a higher possibility for the soft binder (or even some recycling agents if added) to diffuse into the aged mortar, which benefits the long-term performance of the damaged PA [25]. Fig. 12 presents the P_c values of the ST emulsion in different PA specimens at depths with an interval of 5 mm. An obvious gradient characteristic could be observed for each ST condition. As Fig. 12(b) shows, the PA specimen of ST

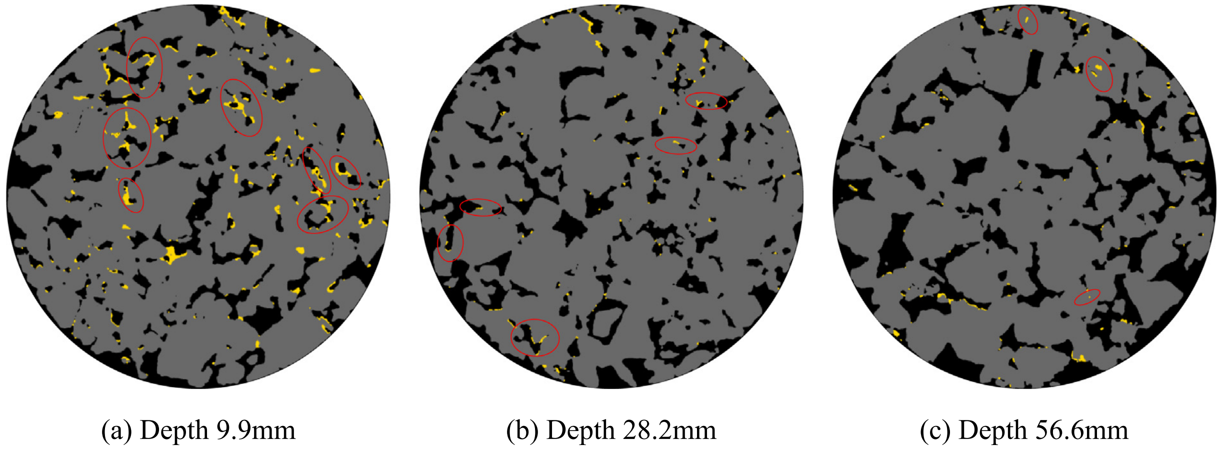

Fig. 9. The RGB images of the back-calculated ST emulsion residue within PA.

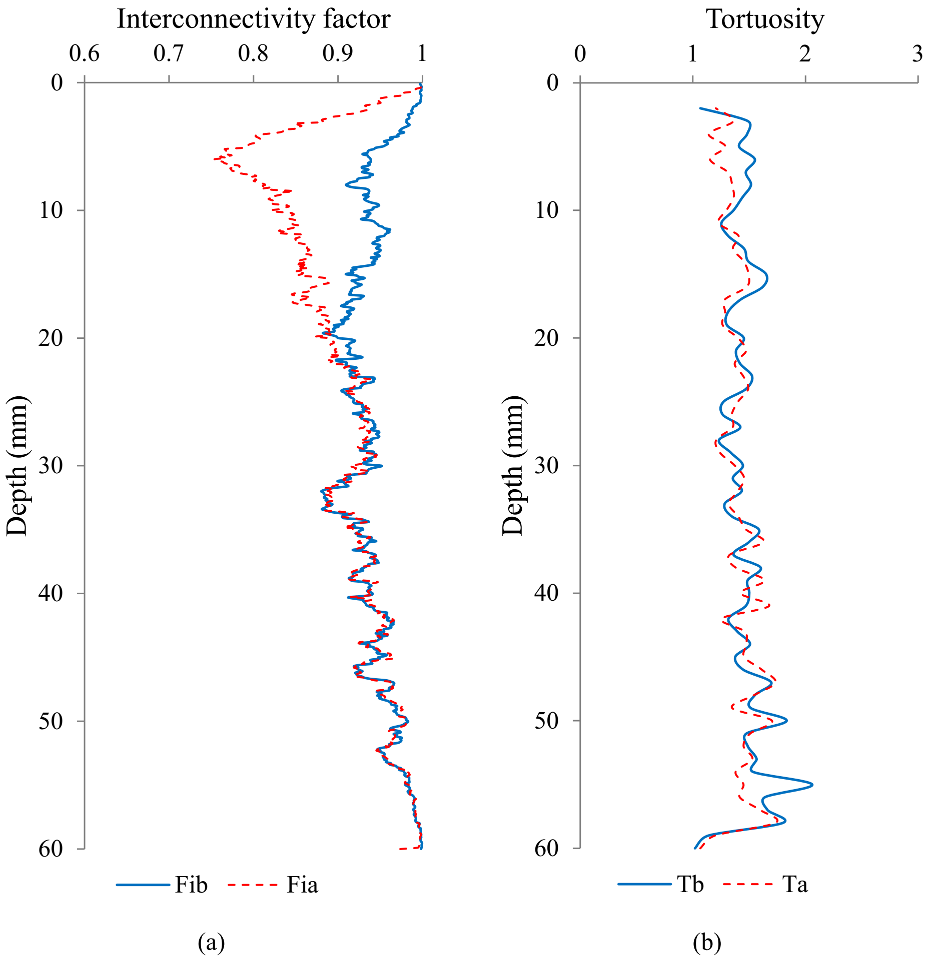

Fig. 10. Interconnectivity and tortuosity of PA before and after ST: (a) F_i; (b) T.

0.6–60% presents the best coating efficiency with P_c value in the range of 6.34% to 36.6%. However, for the ST 0.4–60% and ST 0.6–40% specimens, the P_c values are in the range of 2.50% to 30.41% and 2.71% to 21.53%, respectively. The lower P_c value range indicates an insufficient coating from the ST emulsion residue. It is worth noting that the P_c value could be well correlated with the mass loss ratio as shown in Table 3. Considering the clear physical meaning of P_c index, it shall be a promising micro-scale index to characterize the coating efficiency of ST emulsions in PA. Apart from the coating, it is worth noting that the mechanical bonding between the ST emulsions and pore surfaces are equally important for the raveling resistance improvement of PA.

3.3.3. Binder film thickness distribution

From the 3D visualization, the spatial distribution of the ST emulsion is complex and non-uniform. So, the binder film thick-

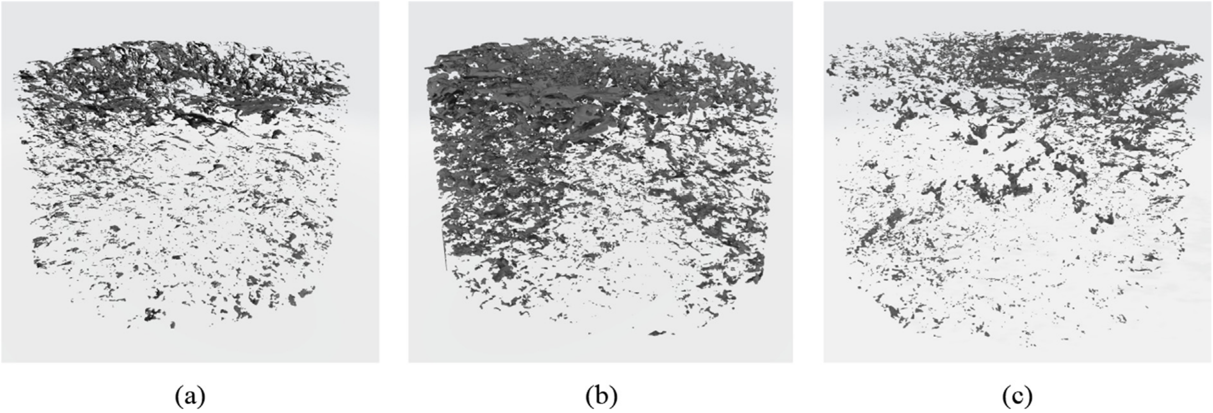

Fig. 11. The back-calculated 3D models of ST emulsion residues of the three ST conditions: (a) ST 0.4–60%; (b) ST 0.6–60%; (c) ST 0.6–40%.

ness distribution of the ST emulsion residue was also evaluated. Fig. 13 shows the frequency histograms of the binder film thickness distribution of the three ST emulsion residues. At each interval (0.1 mm), the frequency is in terms of a percentage of the number of certain coating film thickness to the total number of calculated coating film thickness. The curves present a double-peak pattern with a higher peak at around 0.3 mm and another peak at around 0.7 mm. ST emulsion residue is formed by the breakage of ST emulsion droplets suspended in water. During the demulsification process, water separates from the asphalt droplets, causing flocculation and coalescence of the ST emulsion and finally forming the asphalt emulsion residue with a thickness of a few hundred microns. However, it is noticed that the film thickness distribution of the ST emulsion residue varies from each other.

Two statistical indexes, namely the mean value (T_c) and standard deviation (SD_c), of the emulsion residue film thickness were also calculated as presented in Table 6. A smaller T_c means a thinner coating layer for the aged mortar. A larger SD_c indicates a wider distribution of the thickness value and less uniformity. Noteworthy, the specimen of ST 0.6–60% exhibits the largest T_c and SD_c value, indicating a thicker coating thickness but less uniformity. A thicker coating layer would reduce the aging rate of the mortar film, which is beneficial to the durability of the mixture [42]. Furthermore, to achieve a better coating efficiency, it is expected that

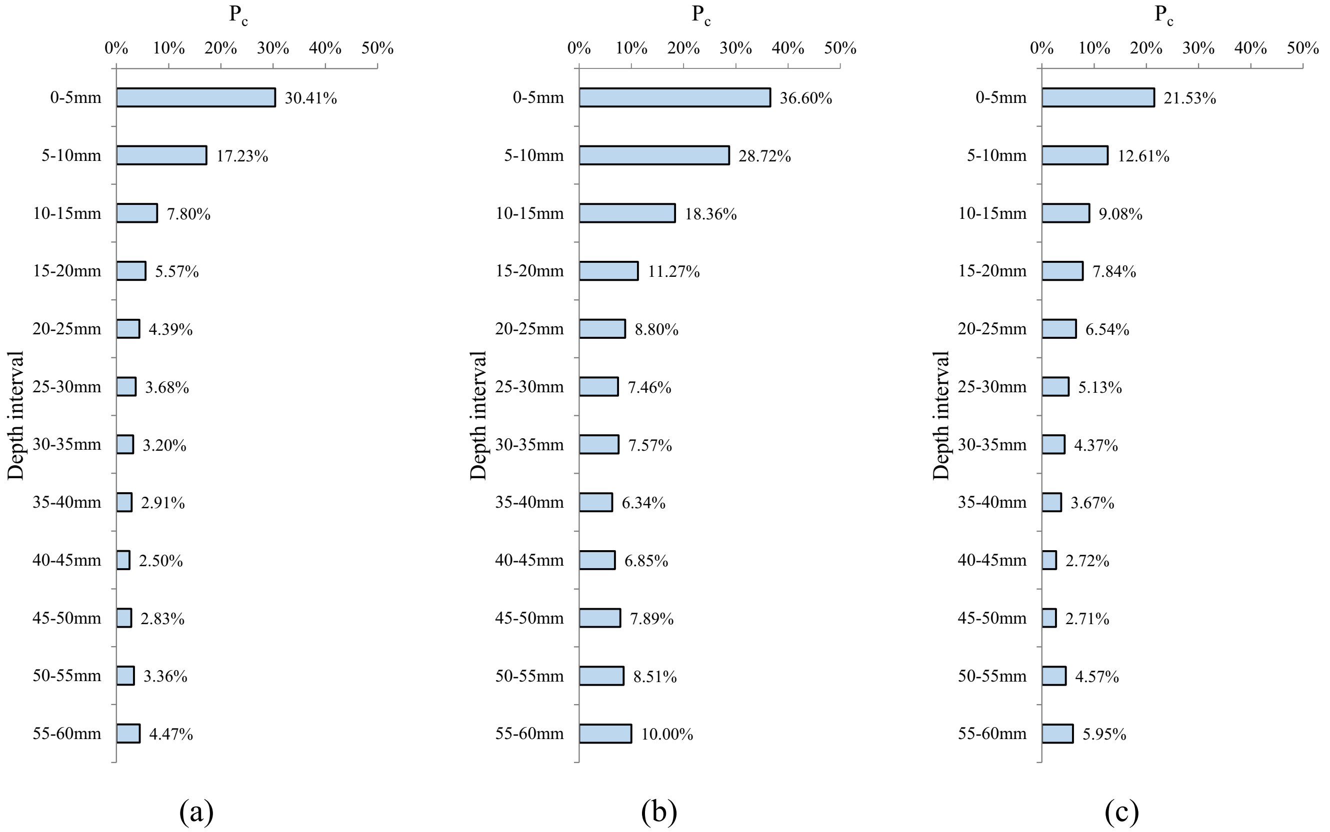

Fig. 12. The P_c value of the ST emulsion at depths for each PA specimen: (a) ST 0.4–60%; (b) ST 0.6–60%; (c) ST 0.6–40%.

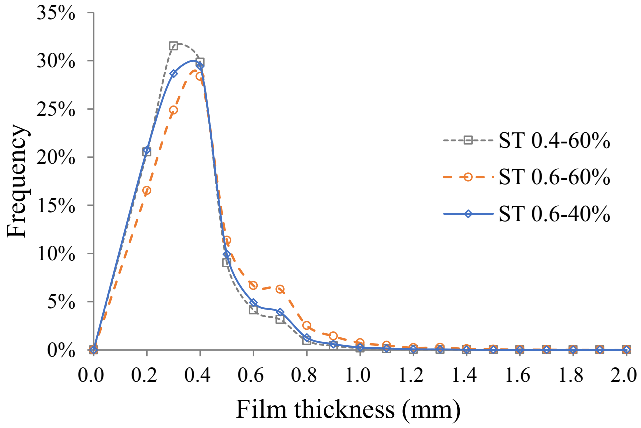

Fig. 13. Binder film distribution curve of the ST emulsion residues.

Table 6
Indexes of the binder film thickness distribution of the ST emulsion residue.

Specimen ID	T_c (mm)	SD_c (mm)
ST 0.4–60%	0.32	0.13
ST 0.6–60%	0.37	0.18
ST 0.6–40%	0.31	0.14

the ST emulsion residue could distribute as uniform as possible, so a smaller SD_c is also preferred.

4. Findings and conclusions

In this study, the 3D models of air voids and ST emulsion residues were reconstructed from the X-ray CT images of the PA specimens before and after ST. The changed pore-microstructure in PA induced by the sprayed ST emulsion was then characterized based on the morphology analysis. The complicated and non-uniform spatial distribution of the ST emulsion residue was quantified by calculating the coating surface area and coating film thickness. Moreover, statistical micro-scale indexes: P_c, T_c and SD_c, were defined to indicate the emulsion residue coating efficiency, mortar thickening and spatial homogeneity, respectively. The following points summarize the main findings and conclusions based on the outcomes of this study:

1) The penetration of the ST emulsion presents gradient characteristics, and the penetration depths of different ST emulsions vary. According to the air void reduction and P_c values, the asphalt emulsion under the ST condition of 0.6–60% had the deepest penetration depth of around 20 mm.
2) The ST application alters the size, number and area distribution of the air voids in PA. Both N_a and D_e reduced at the bottom of each PA specimen after ST, N_a increased while D_e decreased at the top of the specimens. Based on image analysis, the ST emulsion droplets can fill the micro-pores and separate the large air voids into multiple smaller ones.
3) The ST emulsion can considerably lower the interconnected factor (F_i) across the top surface of the PA specimen and the tortuosity (T) at both ends of the specimen. The smaller F_i value should be primarily responsible for the decreased permeability of the PA specimen caused by the ST emulsion.
4) The P_c value has a strong relationship with the mass loss ratio of the treated PA specimen. A larger P_c value implies improved coating effectiveness on the aged mortar surface and, potentially, improved recovery efficiency for the damaged PA.
5) Apart from the P_c value, a thicker (larger T_c value) and more uniform (smaller SD_c value) coating film thickness is also expected for the ST emulsion to achieve a better penetration status in PA.

It is worth noting that the findings above are based on the laboratory tests on certain selected ST emulsion materials and PA materials. To further validate the robustness of the newly proposed micro-scale indices, the penetration behavior of different ST emulsions in different PA specimens from both the laboratory and field coring should be investigated in the future study. Also, the effects of ST emulsion on the function performance of PA, such as noise absorption and water infiltration, will be carefully investigated.

CRediT authorship contribution statement

Jiwang Jiang: Conceptualization, Investigation, Methodology, Writing – original draft. **Zhen Leng:** Conceptualization, Funding acquisition, Validation, Resources. **Bin Yang:** Conceptualization, Investigation, Methodology. **Guoyang Lu:** Validation, Writing – review & editing. **Zhifei Tan:** Methodology. **Meizhao Han:** Investigation. **Zejiao Dong:** Resources, Supervision, Writing – review & editing.

Data availability

The authors are unable or have chosen not to specify which data has been used.

Declaration of Competing Interest

The authors declare that they have no known competing financial interests or personal relationships that could have appeared to influence the work reported in this paper.

Acknowledgement

This work was supported by the Hong Kong Research Grant Council through the GRF project (Grant No. 15209920), and PolyU Postdoctoral Fellowship Scheme (Grant No. G-YW5E).

References

[1] A.E. Alvarez, A.E. Martin, C. Estakhri, A review of mix design and evaluation research for permeable friction course mixtures, Constr. Build. Mater. 25 (3) (2011) 1159–1166.
[2] R. Cao, Z. Leng, J. Yu, S.-C. Hsu, Multi-objective optimization for maintaining low-noise pavement network system in Hong Kong, Transport. Res. Part D, Transport Environ. 88 (2020) 102573.
[3] G. Dell'acqua, M. De Luca, R. Lamberti, Indirect Skid Resistance Measurement for Porous Asphalt Pavement Management, Transp. Res. Rec. 2205 (1) (2011) 147–154.
[4] E.S.H. Garcia, L.P. Thives, E. Ghisi, L.N. Antunes, Analysis of permeability reduction in drainage asphalt mixtures due to decrease in void volume, J. Cleaner Prod. 248 (2020) 119292.
[5] Y. Liu, T. Li, L. Yu, Urban heat island mitigation and hydrology performance of innovative permeable pavement: A pilot-scale study, J. Cleaner Prod. 244 (2020) 118938.
[6] X. Wang, X. Gu, J. Jiang, H. Deng, Experimental analysis of skeleton strength of porous asphalt mixtures, Constr. Build. Mater. 171 (2018) 13–21.
[7] A.A.A. Molenaar, E.T. Hagos, M.F.C. van de Ven, Effects of Aging on the Mechanical Characteristics of Bituminous Binders in PAC, J. Mater. Civ. Eng. 22 (8) (2010) 779–787.
[8] L. Ma, A. Varveri, R. Jing, S. Erkens, Comprehensive review on the transport and reaction of oxygen and moisture towards coupled oxidative ageing and moisture damage of bitumen, Constr. Build. Mater. 283 (2021) 122632.
[9] N. Kringos, A. Scarpas, Raveling of Asphaltic Mixes Due to Water Damage: Computational Identification of Controlling Parameters, Transp. Res. Rec. 2005 (1929) 79–87.
[10] K. Zhang, J. Kevern, Review of porous asphalt pavements in cold regions: The state of practice and case study repository in design, construction, and maintenance, J. Infrastructure Preservation Resilience 2 (1) (2021) 1–17.

[11] M. Ameri, M.A. Esfahani, Evaluation and Performance of Hydrated Lime and Limestone Powder in Porous Asphalt, Road Mater. Pavement Des. 9 (4) (2008) 651–664.
[12] F. Gu, R. Moraes, C. Chen, F. Yin, D. Watson, A. Taylor, Effects of Additional Antistrip Additives on Durability and Moisture Susceptibility of Granite-Based Open-Graded Friction Course, J. Mater. Civ. Eng. 33 (9) (2021) 4021245.
[13] J. Cai, C. Song, B. Zhou, Y. Tian, R. Li, J. Zhang, J. Pei, Investigation on high-viscosity asphalt binder for permeable asphalt concrete with waste materials, J. Cleaner Prod. 228 (2019) 40–51.
[14] S. Shimeno, A. Oi, T. Tanaka, Evaluation and further development of porous asphalt pavement with 10 years experience in Japanese expressways, Proceedings of the 11th International Conference on Asphalt Pavements (2010) 43-52, Nagoya.
[15] R. Cao, Z. Leng, S.-C. Hsu, W.-T. Hung, Modelling of the pavement acoustic longevity in Hong Kong through machine learning techniques, Transport. Res. Part D, Transport Environ. 83 (2020) 102366.
[16] Z. Leng, R.K. Padhan, A. Sreeram, Production of a sustainable paving material through chemical recycling of waste PET into crumb rubber modified asphalt, J. Cleaner Prod. 180 (2018) 682–688.
[17] T. Törzs, G. Lu, A.O. Monteiro, D. Wang, J. Grabe, M. Oeser, Hydraulic properties of polyurethane-bound permeable pavement materials considering unsaturated flow, Constr. Build. Mater. 212 (2019) 422–430.
[18] G. Lu, P. Liu, Y. Wang, S. Faßbender, D. Wang, M. Oeser, Development of a sustainable pervious pavement material using recycled ceramic aggregate and bio-based polyurethane binder, J. Cleaner Prod. 220 (2019) 1052–1060.
[19] G. Lu, H. Wang, Y. Zhang, P. Liu, D. Wang, M. Oeser, J. Grabe, The hydro-mechanical interaction in novel polyurethane-bound pervious pavement by considering the saturation states in unbound granular base course, Int. J. Pavement Eng. (2021) 1–14.
[20] J.P. Wu, P.R. Herrington, D. Alabaster, Long-term durability of epoxy-modified open-graded porous asphalt wearing course, Int. J. Pavement Eng. 20 (8) (2019) 920–927.
[21] J. Santos, G. Flintsch, A. Ferreira, Environmental and economic assessment of pavement construction and management practices for enhancing pavement sustainability, Resour. Conserv. Recycl. 116 (2017) 15–31.
[22] L. Yao, Q. Dong, J. Jiang, F. Ni, Deep reinforcement learning for long-term pavement maintenance planning, Comput.-Aided Civ. Infrastruct. Eng. 35 (11) (2020) 1230–1245.
[23] M.F.C. van de Ven, J. Qiu, Y. Zhang, Increasing the functional service life of porous surfacings: Development of test methods to study the effect of rejuvenating binders, Proceeding of 15th International Flexible Pavements Conference of AAPA, Australian Asphalt Pavement Association (2013), Queensland, Australia.
[24] Y. Zhang, M.F.C. van de Ven, A.A.A. Molenaar, S. Wu, Assessment of Effectiveness of Rejuvenators on Artificially Aged Mortar, J. Mater. Civ. Eng. 28 (9) (2016) 4016079.
[25] Y. Zhang, Z. Leng, Quantification of bituminous mortar ageing and its application in ravelling evaluation of porous asphalt wearing courses, Mater. Des. 119 (2017) 1–11.
[26] B. Xu, M. Li, S. Liu, J. Fang, R. Ding, D. Cao, Performance analysis of different type preventive maintenance materials for porous asphalt based on high viscosity modified asphalt, Constr. Build. Mater. 191 (2018) 320–329.
[27] J. Hu, Z. Qian, P. Liu, D. Wang, M. Oeser, Investigation on the permeability of porous asphalt concrete based on microstructure analysis, Int. J. Pavement Eng. 21 (13) (2020) 1683–1693.
[28] M. Aboufoul, N. Shokri, E. Saleh, C. Tuck, A. Garcia, Dynamics of water evaporation from porous asphalt, Constr. Build. Mater. 202 (2019) 406–414.
[29] Ministry of Transport of China, Technology specifications for design and construction of porous asphalt pavement (JTG/T 3350–03-2020), China Communications Press (2020), China (in Chinese).
[30] Y. Zhang, H. Chen, H.U. Bahia, Extended aging performance of high RAP mixtures and the role of softening oils, Int. J. Pavement Eng. 23 (8) (2022) 2773–2784.
[31] AASHTO (American Association of State Highway and Transportation Officials), Standard method of test for resistance of compacted asphalt mixtures to moisture-induced damage. AASHTO T283 (2014), Washington, DC: AASHTO.
[32] ASTM C131, Standard test method for resistance to degradation of small-size coarse aggregate by abrasion and impact in the los angeles machine, ASTM International, West Conshohocken, PA, 2020.
[33] EN 12697-19, Bituminous mixtures - test methods - Part 19: Permeability of specimen, European Committee for Standardization, Brussels, Belgium, 2020.
[34] X. Ma, J. Jiang, Y. Zhao, H. Wang, Characterization of the interconnected pore and its relationship to the directional permeability of porous asphalt mixture, Constr. Build. Mater. 269 (2021) 121233.
[35] Y. Zhao, X. Wang, J. Jiang, L. Zhou, Characterization of interconnectivity, size distribution and uniformity of air voids in porous asphalt concrete using X-ray CT scanning images, Constr. Build. Mater. 213 (2019) 182–193.
[36] J. Jiang, F. Ni, X. Gu, L. Yao, Q. Dong, Evaluation of aggregate packing based on thickness distribution of asphalt binder, mastic and mortar within asphalt mixtures using multiscale methods, Constr. Build. Mater. 222 (2019) 717–730.
[37] E. Masad, V.K. Jandhyala, N. Dasgupta, N. Somadevan, N. Shashidhar, Characterization of Air Void Distribution in Asphalt Mixes using X-ray Computed Tomography, J. Mater. Civ. Eng. 14 (2) (2002) 122–129.
[38] M.R. Mitchell, R.E. Link, A.E. Alvarez, A. Epps Martin, C. Estakhri, Connected Air Voids Content in Permeable Friction Course Mixtures, J. Test. Eval. 37 (3) (2009) 102056.
[39] B. Schuck, T. Teutsch, S. Alber, W. Ressel, H. Steeb, M. Ruf, Study of air void topology of asphalt with focus on air void constrictions–a review and research approach, Road Mater. Pavement Des. 22 (sup1) (2021) S425–S443.
[40] Z. Wang, J. Xie, L. Gao, Y. Tan, K. Li, Study on sound absorption model of porous asphalt concrete based on three-dimensional morphology of air voids, Constr. Build. Mater. 338 (2022) 127537.
[41] S. Alber, W. Ressel, P. Liu, J. Hu, D. Wang, M. Oeser, D. Uribe, H. Steeb, Investigation of microstructure characteristics of porous asphalt with relevance to acoustic pavement performance, Int. J. Transp. Sci. Technol. 7 (3) (2018) 199–207.
[42] J. Jiang, Y. Li, Y. Zhang, H.U. Bahia, Distribution of mortar film thickness and its relationship to mixture cracking resistance, Int. J. Pavement Eng. 23 (3) (2022) 824–833.